

Deep redshift topological lensing: strategies for the T^3 candidate

Boudewijn F. Roukema^{1,2}, Martin J. France², Tomasz A. Kazimierczak¹, and Thomas Buchert²

¹ Toruń Centre for Astronomy, Faculty of Physics, Astronomy and Informatics, Nicolaus Copernicus University, ul. Gagarina 11, 87-100 Toruń, Poland

² Université de Lyon, Observatoire de Lyon, Centre de Recherche Astrophysique de Lyon, CNRS UMR 5574: Université Lyon 1 and École Normale Supérieure de Lyon, 9 avenue Charles André, F-69230 Saint-Genis-Laval, France*

Le 19 février 2013

ABSTRACT

Context. The 3-torus (T^3) Friedmann-Lemaître-Robertson-Walker (FLRW) model better fits the nearly zero large-scale two-point auto-correlation of the Wilkinson Microwave Anisotropy Probe (WMAP) cosmic microwave background (CMB) sky maps than the infinite flat model. The T^3 model's parameters, recently found using an optimal cross-correlation method on WMAP data, imply approximately equal-redshift topological lensing at redshifts $z \sim 6$, the redshift range of the upcoming generation of new instruments and telescopes.

Aims. We investigate observational strategies that can reject the T^3 solution for a given region of parameter space of physical assumptions, or provide good candidate topologically lensed galaxy pairs for detailed spectroscopic followup.

Methods. T^3 holonomies are applied to (i) existing $z \sim 6$ observations and (ii) simulated observations, creating multiply connected catalogues. Corresponding simply connected catalogues are generated. The simulated observational strategies are motivated by the matched discs principle. Each catalogue is analysed using a successive filter method and collecting matched quadruples. Quadruple statistics between the multiply and simply connected catalogues are compared.

Results. The expected rejection of the hypothesis, or detection of candidate topologically lensed galaxies, is possible at a significance of 5% for a pair of T^3 axis-centred northern and southern surveys if photometric redshift accuracy is $\sigma(z_{\text{phot}}) \lesssim 0.01$ for a pair of nearly complete 100 deg^2 surveys with a total of $\gtrsim 500$ galaxies over $4.3 < z < 6.6$, or for a pair of 196 deg^2 surveys with $\gtrsim 400$ galaxies and $\sigma(z_{\text{phot}}) \lesssim 0.02$ over $4 < z < 7$. Dropping the maximum time interval in a pair from $\Delta t = 1 \text{ h}^{-1} \text{ Gyr}$ to $\Delta t = 0.1 \text{ h}^{-1} \text{ Gyr}$ requires $\sigma(z_{\text{phot}}) \lesssim 0.005$ or $\sigma(z_{\text{phot}}) \lesssim 0.01$, respectively.

Conclusions. Millions of $z \sim 6$ galaxies will be observed over fields of these sizes during the coming decades, implying much stronger constraints. The question is not *if* the hypothesis will be rejected or confirmed, it is *when*.

Key words. cosmology: observations – cosmological parameters – Galaxies: high-redshift — distance scale

1. Introduction

The predictions implied by cosmic topology interpretations of the lack of large-scale (hereafter, $r \gtrsim 10 h^{-1} \text{ Gpc}$) structure in the cosmic microwave background (CMB) maps are relevant for the design of deep redshift observational strategies. The large-scale structures in the CMB as observed by the COsMIC Background Explorer (COBE) and the WILKINSON MICROWAVE ANISOTROPY PROBE (WMAP) (Bennett et al. 2003), i.e., in particular, the second moment of the temperature fluctuation distribution, can be statistically analysed using either (i) spherical harmonics analysis of the temperature fluctuations, which is invalid if observations near the galactic plane are contaminated, or (ii) the angular or spatial two-point auto-correlation function of the temperature fluctuations. (The full moment hierarchy can be estimated using Minkowski functionals of iso-temperature excursion sets (Schmalzing & Buchert 1997; Schmalzing & Gorski 1998; Ducout et al. 2012).) Interpreting the (second moment) large-scale harmonics to be generated by statistically independent Gaussian distributions requires an unlikely “conspiracy” between the harmonics at low l values (Copi et al. 2007, 2009; Sarkar et al. 2011; Copi et al. 2010) in order to match the nearly zero value of the (two-point) auto-correlation function at large ($r \gtrsim r_{\text{SLS}} \approx 10.0 h^{-1} \text{ Gpc}$) pair separations (Sect. 7, Fig. 16

Spergel et al. 2003; also Fig. 1 Roukema et al. 2008b) where r_{SLS} is the comoving distance to the surface of last scattering (SLS). Thus, Occam's razor suggests that an approximately zero large-scale auto-correlation function provides a simpler statistical model for the largest scales than the harmonic analysis.

The Friedmann-Lemaître-Robertson-Walker (FLRW) models of the Universe assume that the comoving spatial section is a 3-manifold, having both curvature and topology (e.g., de Sitter 1917; Friedmann 1923, 1924; Lemaître 1927; Robertson 1935).¹ For recent reviews and terminology such as “fundamental domain”, “covering space”, and “topological lensing” (where the topology of a spatial section of the Universe can be thought of as a “lens”, in analogy with gravitational lensing), see e.g., Lachièze-Rey & Luminet (1995); Luminet (1998); Starkman (1998); Luminet & Roukema (1999); Rebouças & Gomero (2004), or shorter, Roukema (2000); Luminet (2006).

Structures bigger than the fundamental domain of an FLRW model (i.e. of the 3-manifold of the comoving spatial section) cannot physically exist, so observations that are most easily interpreted in the universal covering space (apparent space) should approximately reveal this (Starobinsky 1993; Stevens et al. 1993; though see also Fig. 1, Roukema 1996). Thus,

¹ See Lemaître (1931) for an English translation of Lemaître (1927), with Lemaître's observational estimate $H_0 \approx 600 \text{ km/s/Mpc}$ excluded (e.g. van den Bergh 2011; Block 2011).

* BFR: during visiting lectureship.

Table 1. Preferred fundamental directions $1 \leq i \leq 6$ of the Aurich (2008) T^3 solution in galactic coordinates^a, with a directional uncertainty of $\sim 2^\circ$ (great circle degrees).

i	1	2	3	4 ^b	5 ^b	6 ^b
unit						
$l_i^{T^3}$	$^\circ$	6	17	107	186	197
$b_i^{T^3}$	$^\circ$	77	-13	3	-77	13
L^{T^3}	c/H_0	3.80 ± 0.05^c				

Notes. ^(a) The typographical error (sign of $b_6^{T^3}$) in Table 1 of Aurich (2008) has been corrected (cf Figs 6, 7 of Aurich 2008).

^(b) The directions 4, 5, and 6 are exactly antipodal to the directions 1, 2, and 3, respectively, and are listed for convenience only.

^(c) Mean and standard error adopted from our analysis (2.1).

the simpler interpretation of the large-scale CMB observations is that the Universe is a multiply connected FLRW model rather than a simply connected FLRW model: the near-zero large-scale two-point auto-correlation reveals the size of the Universe. Among the models that are considered to provide better fits to the WMAP data than the infinite flat model are the Poincaré dodecahedral space (S^3/I^* , Luminet et al. 2003; Aurich et al. 2005a, 2005b; Gundermann 2005; Caillerie et al. 2007; Roukema et al. 2008b, 2008a), the Picard space ($H^3/\text{PSL}_2(\mathbb{Z}[i])$, Picard 1884; Aurich et al. 2004), the regular 3-torus (T^3 , Spergel et al. 2003; Aurich et al. 2007; Aurich 2008; Aurich et al. 2008, 2010), and the “2-torus” ($S^1 \times S^1 \times \mathbb{R}$, Aslanyan & Manohar 2012), though some analyses, also assuming an FLRW (homogeneous) metric, favour the infinite flat model (Key et al. 2007; Niarchou & Jaffe 2007; Bielewicz & Banday 2011).

While there is a lack of consensus in fitting models to the WMAP data, the T^3 model fits have a particular advantage from an observational point of view: they imply sub-SLS topological lensing at redshifts that are becoming observationally realistic. Many cosmic topology CMB analyses consider ensembles of possible sizes and orientations of the fundamental domain of a given model. A more empirical approach requires that the fundamental domain of the real Universe must have a specific size and orientation in astronomical coordinates. We live in a specific realisation of the physical processes that led to our Universe, not an ensemble of realisations. Aurich (2008) applied the optimal cross-correlation method (Roukema et al. 2008b, 2008a) to find a specific T^3 solution. This solution implies equal-redshift topological lensing at redshifts $z \gtrsim 6$, the redshift range at which many detections are expected with the upcoming generation of new instruments and telescopes. Thus, this candidate 3-manifold is, in principle, empirically testable independently of the CMB.

Roukema & Kazimierczak (2011) presented a corollary of the matched circles principle (Cornish et al. 1996, 1998): the *matched discs* principle. In general, topologically lensed pairs of images of a given physical object occur at different redshifts. This complicates observational tests: the lifetimes of quasars are short compared to typical differences in lookback times, and at high redshifts, a galaxy seen in one direction at a redshift of z_1 may be absent at an expected position with a higher redshift $z_2 > z_1$ because the initial starburst occurs after z_2 and before z_1 . Matched discs minimise this problem, by selecting the set of spatial positions—discs—for which a topologically lensed pair of any given galaxy occurs at identical redshifts in the two matched discs (Fig. 1, Roukema & Kazimierczak 2011).

The redshift is lowest at the centre of a disc and increases radially outwards. The Poincaré dodecahedral space matched discs occur with $z_{\min} = 106 \pm 18$, so detection of gravitationally collapsed objects (galaxies) would require the existence and detection of rare high overdensity peaks of the density fluctuation distribution that collapsed very early. In contrast, the Aurich (2008) T^3 candidate has $z_{\min} \sim 5$ (Fig. 10, Sect. 3, Aurich 2008). While relatively small numbers of quasars have been detected with $z \gtrsim 5$, many Lyman break galaxies (LBGs) and Lyman alpha emitters (LAEs) in this redshift range have now been observed [with spectroscopic confirmations up to $z = 8.6$ (Lehnert et al. 2010)] and many more are likely to be detected with the new instruments and telescopes of the coming decade. LBGs and LAEs have a topological lensing advantage over quasars: the emission from a given object is expected to be much more isotropic than the beamed jets of a quasar, and the lifetime is likely to be much longer, because of long galaxy dynamical time scales and stellar lifetimes.

Thus, the Aurich (2008) solution is going to be testable over matched discs of many square degrees using observations to be made over the next few years (e.g., VISTA/VIKING, Subaru/CISCO, EUCLID, VLT/X-Shooter, VLT/MUSE, JWST; see Sect. 2.2.2 for details). Although surveys that are approximately limited to a narrow band in redshift correspond to thin shells rather than thin discs, surveys over solid angles $\ll 4\pi$ (e.g. many square degrees) can strongly overlap with matched discs if made over the predicted redshift ranges. Since observational and theoretical uncertainties in the candidate 3-manifold cannot be avoided, a successive filter method for finding sets of likely topologically lensed pairs (Roukema 1996; Uzan et al. 1999; Marecki et al. 2005; Fujii & Yoshii 2011) is preferable to the pair separation histogram (PSH) method (Lehoucq et al. 1996), as the former can reveal very weak topological lensing signals (Fujii & Yoshii 2011). Here, a successive filter method, motivated by the matched discs principle, is applied to existing observational data and planned or possible surveys, using numerical simulations, in order to investigate observational strategies that can reject the T^3 solution, on the assumption that the FLRW metric is close enough to physical reality.

In Sect. 2.1, we briefly present the Aurich (2008) T^3 solution, matched discs, and not-quite-matched beams. Existing and planned or possible observations that can be used to predict sky positions and redshifts of topologically lensed copies are presented in Sect. 2.2. For existing observations, we apply the successive filter method to two partly simulated catalogues. The signal is represented by analysing the union of the observational catalogue with its topologically lensed images on (approximately) the opposite side(s) of the sky. Noise is represented by analysing the union of the observational catalogue with a simulated (non-lensed) data set in the region of comoving space where lensed objects would be found. Thus, signal is compared to noise. For planned or possible observations, the data are fully simulated, comparing a multiply connected T^3 simulation with a simply connected \mathbb{R}^3 simulation. The simulation methods are described in Sect. 2.3, and the successive filter method is presented in Sect. 2.4. Statistical tests, either to find a low probability of falsely excluding the T^3 hypothesis, or to find a low probability of falsely detecting evidence in favour of the hypothesis, are presented in Sect. 2.5.

Results are presented in Sect. 3 and conclusions are given in Sect. 4. All distances are FLRW comoving distances except if stated otherwise, and Ω_m and Ω_Λ are the dimensionless matter density and dark energy density, respectively. The Hubble con-

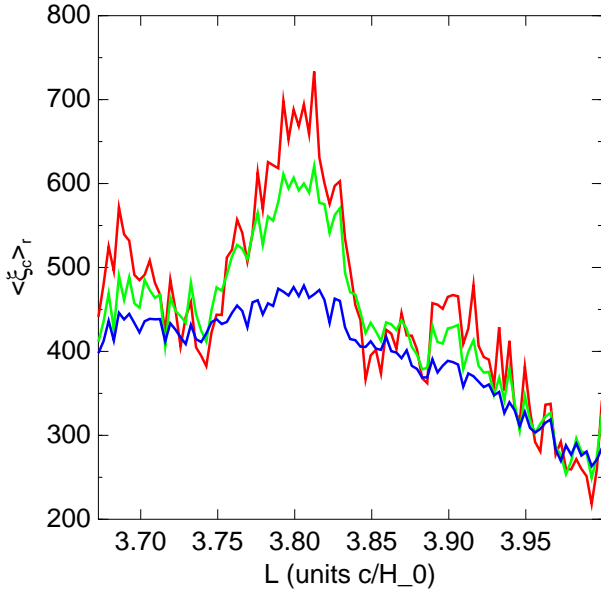


Fig. 1. Sub-gigaparsec-scale mean cross-correlation $\langle \xi_C \rangle_r(L)$ [Eq. (1)] in μK^2 as a function of Universe size L^{T^3} in units of c/H_0 , for the WMAP 9-year ILC map using the KQ85 galactic mask, for $r = 0.2, 0.4, 1.0 h^{-1}$ Gpc from top to bottom (red, green, blue, respectively, online), for the orientation given in Table 1.

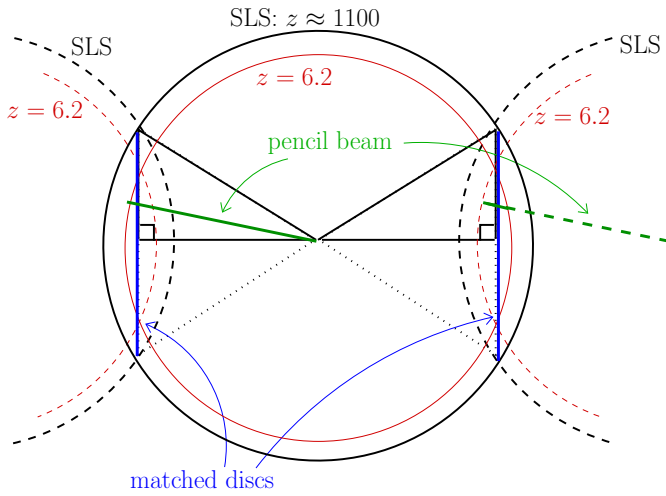


Fig. 2. Matched discs in the universal covering space, as per Fig. 1, Roukema & Kazimierczak (2011), but for the Aurich (2008) T^3 solution, with the addition of matched pencil beam observations. Spheres corresponding to an example redshift $z = 6.2$ are shown intersecting themselves (in the covering space). The redshift at the centres of the matched discs is less than this, and within a disc, the redshift increases radially out to the surface of last scattering (SLS). An observer (at the centre) pointing a telescope towards the right-hand matched disc can observe the $z \lesssim 6.2$ portion of the right-hand copy of the pencil beam at roughly the same redshifts as those of the corresponding portion of the left-hand copy of the pencil beam.

Table 2. Redshifts increasing radially outwards from the centre of matched discs for the Aurich (2008) T^3 solution, but with $L^{T^3} = 3.8$ motivated by the WMAP7 ILC map (Fig. 1), at angle β from the disc centre, and approximate fraction of full sky covered by the three pairs of discs $\omega/(4\pi)^a$, depending on the assumed FLRW metric parameter Ω_m , where $\Omega_\Lambda = 1 - \Omega_m$.

$\Omega_m =$	0.26	0.27	0.28	0.29	0.30	
β	z					$\omega/(4\pi)$
$^\circ$						
0	4.98	5.17	5.35	5.55	5.75	0%
5	5.04	5.22	5.42	5.61	5.82	1%
10	5.21	5.41	5.61	5.82	6.04	5%
10^b	6.10	6.36	6.63	6.92	7.21	5%
15	5.52	5.74	5.96	6.20	6.45	10%
20	6.02	6.27	6.53	6.81	7.10	18%
25	6.78	7.1	7.42	7.77	8.13	28%
30	7.99	8.41	8.85	9.31	9.81	40%

Notes. ^(a) Galactic masking would modify these rough estimates.

^(b) Calculation assuming $L^{T^3} = 4.0$ for the circle with $\beta = 10^\circ$, to illustrate the effect of uncertainty in L^{T^3} .

2. Method

2.1. The Aurich (2008) T^3 solution, matched discs, and not-quite-matched beams

The coordinates of the Aurich (2008) T^3 solution are given in Table 1. We check the cross-correlation ξ_C (Roukema et al. 2008b) on the 9-year WMAP internal linear combination (ILC) map², using the corresponding KQ85 galactic contamination mask,³ and show the dependence of the sub-gigaparsec-scale mean cross-correlation

$$\langle \xi_C \rangle_r(L) := \frac{1}{r} \int_0^r \xi_C(r', L) dr' \quad (1)$$

in Fig. 1. The cross-correlation ξ_C is a two-point correlation function that at small scales correlates pairs of points that are observed to be separated by large distances but according to the hypothesised 3-manifold are also separated by a small distance. The cross-correlation should be low if the hypothesis is wrong (Fig. 2 Roukema et al. 2008b) and high if the hypothesis is correct (Fig. 3 Roukema et al. 2008b). The strongest cross-correlation in Fig. 1 occurs for $L^{T^3} \approx 3.80 \pm 0.05$ (in units of c/H_0), where the uncertainty is the half-width of the maximum at its base. The Aurich (2008) uncertainties are estimated from the pseudo-probability function used in the Monte Carlo Markov Chain search for an optimal solution. Since the pseudo-probability estimator is not a true probability, other methods are needed to estimate a realistic uncertainty. Figure 9 of Aurich (2008), showing the estimates in different foreground-subtracted single waveband WMAP maps, suggests $\sigma(L^{T^3}) \approx 0.02$, combining random and some systematic sources of error (ILC versus single band maps). The shift by $0.05(c/H_0)$ between Aurich (2008)'s estimate of L^{T^3} for WMAP5 data and that shown

² http://lambda.gsfc.nasa.gov/data/map/dr5/dfp/ilc/wmap_ilc_9yr_v5.fits

³ The 9-year version of the KQ85 mask http://lambda.gsfc.nasa.gov/data/map/dr5/ancillary/masks/wmap_temperature_kq85_analysis_mask_r9_9yr_v5.fits hides about 25.2% of the sky.

stant is written $H_0 = 100h$ km/s/Mpc and c is the conversion factor from time units to space units.

in Fig. 1 suggests that inclusion of systematic error would give $\sigma(L^{T^3}) \gtrsim 0.05$, i.e. $150h^{-1}$ Mpc, rather than $\sigma(L^{T^3}) = 0.02$. The angular uncertainty given by Aurich (2008), 2° , is similar to that of the Poincaré dodecahedral space solution found earlier with the optimal cross-correlation method (Roukema et al. 2008b, 2008a), i.e. a few hundred comoving h^{-1} Mpc in a tangential direction at a radial distance of 5 to 10 h^{-1} Gpc.

Leaving aside these uncertainties for the moment, the observationally most dramatic element of this T^3 solution is revealed by considering the redshift of an object topologically lensed in opposite directions along a fundamental axis. Aurich (2008) shows this in his Fig. 10 and briefly discusses it. Here, we use the principle of matched discs (Roukema & Kazimierczak 2011), shown with some extra detail in Fig. 2, and Table 2, listing the redshifts at the centres of a pair of matched discs and at circles increasing radially outwards to form the pair of matched discs. The fractional sky coverage $\omega/(4\pi) = 12\pi(1 - \cos\beta)/(4\pi)$, for discs of angular radius β , is also shown.

Given the rapidly increasing numbers of observed objects in the $5 \lesssim z \lesssim 6$ range, the beginning of detections around $6 \lesssim z \lesssim 8$, and the large fractional covering of the sky by the matched discs, it is obvious that independently of the few hundred h^{-1} Mpc uncertainties in the T^3 solution, the observational data to reject or confirm the solution to very high statistical significance are going to become available over the next decade or two. The absence of topologically lensed images of quasars can be interpreted as a problem of their short lifetimes and highly anisotropic nature (beamed jets), but the absence of topologically lensed images of early forming galaxies would be much more difficult to explain.

Let us return to the uncertainty in the T^3 solution parameters. Pencil beam observations (“deep fields”) that probe to $z \sim 6$ have typical widths of at most a few arcminutes, i.e. a few h^{-1} Mpc in comoving thickness at these redshifts. Thus, an accuracy of a few hundred h^{-1} Mpc suggests that deep fields of a few degrees in size—pointed in the appropriate directions—will most likely be needed. The fourth row of entries in Table 2 shows the redshifts at the $\beta = 10^\circ$ radius circle for $L^{T^3} = 4.0$, i.e. 4σ greater than the WMAP9-ILC estimate shown in Fig. 1 if σ is defined as the absolute difference between the Aurich (2008) WMAP5 estimate and the WMAP9-ILC estimate made here. Thus, for surveys limited to, e.g. $z < 6.2$, observations closer to the face centres would better test the solution.

Figure 2 also shows a pair of not-quite-matched beams. These are not truly matched, since they exactly match only where they intersect the matched discs. The topologically matched parts of the two beams to the left (in Fig. 2) of their respective discs occur in the left-hand copy of the beam at slightly higher redshifts and in the right-hand copy at slightly lower redshifts, with respect to the redshift of the intersections with the matched discs. Since realistic surveys usually have wide redshift distributions, there is a fair chance of covering the topologically lensed region. However, this requires that the survey of the right-hand copy (in this figure) of the beam be wide enough in solid angle to cover the projection of the “beam” onto the sky, since the right-hand copy is not a beam from the observer’s point of view. For a small angular distance of the left-hand copy of the beam from the matched disc centre, the projected solid angle of a small portion of the right-hand copy will not be too large. Thus, for a small angular offset from the matched disc centres (axes of the fundamental domain), “not-quite-matched beams” can potentially test topological lensing hypotheses.

While matched discs and not-quite-matched beams indicate the parts of the sky that should be observed, detecting a signif-

Table 3. Number of astrophysical objects with $5 \leq z \leq 6.2$ and within 10° of the Aurich (2008) T^3 solution fundamental axes (numbered as in Table 1) listed in NED^a as of 28 Oct 2012.

i	1	2	3	4	5	6
NED count	44	0	0	9	1	0

Notes. ^(a) NASA/IPAC Extragalactic Database, (<http://ned.ipac.caltech.edu>)

Table 4. Some well-known deep fields and their angular distance θ_i from the nearest T^3 axis (listed if $\theta \leq 20^\circ$).

name unit	l °	b °	$\min_{i=1}^6(\theta_i)$ °	l_{T^3} °	b_{T^3} °
VVDS 0226–04 ^a	172.	–58.	20.	186.	–77.
CDFS ^b	224.	–54.	26.		
HDF-S ^c	328.	–49.	52.		
VVDS 2217+00 ^a	63.	–44.	50.		
VVDS 1003+01 ^a	238.	43.	46.		
HDF ^d	126.	55.	43.		
AEIS ^e	97.	60.	33.		
VVDS 1400+05 ^f	343.	63.	16.	6.	77.
SDF ^g	38.	83.	8.	6.	77.

Notes. ^(a) VIRMOS Very Deep Survey (Le Fèvre et al. 2003)

^(b) Chandra Deep Field South

(http://www.eso.org/~vmainier/cdfs_pub/CDFSfield.html)

^(c) Hubble Deep Field-South “WPFC2 (apex) pointing”

(<http://www.stsci.edu/ftp/science/hdfsouth/coordinatesS.html>)

^(d) Hubble Deep Field (Williams et al. 1996)

^(e) All-Wavelength Extended Groth Strip International Survey (Davis et al. 2007)

^(f) Iovino et al. (2005)

^(g) Subaru Deep Field (Maihara et al. 2001)

icant statistical signal and generating a list of candidate pairs of topologically lensed objects requires a sensitive statistical method. This is presented below in Sect. 2.4. However, first we need to consider existing, planned and possible surveys in the three-dimensional regions of interest.

2.2. Observational catalogues

2.2.1. Existing observations

Table 3 shows that almost all of the $z \sim 6$ objects that are so far known near the T^3 axes are those near the high galactic latitude, northern fundamental direction 1, although a few are also known near the corresponding southern fundamental direction 4. Most of the northern objects are from the Subaru Deep Field observed with the Cooled Infrared Spectrograph and Camera for [the] OH airglow suppressor (CISCO) on the 8.2 m Subaru telescope (Maihara et al. 2001; Shimasaku et al. 2006), listed along with some of the other well-known deep fields in Table 4. The galactic coordinates and redshifts of the northern objects are listed as part of Table 5.

Table 5. Known objects^a near the northern galactic matched disc at sky position (l_1, b_1) and redshift z_1 and their predicted most likely southern galactic positions (l_2, b_2) and redshifts z_2 , and redshift and cosmological time differences $\Delta z := z_1 - z_2$ and $\Delta t := t_2 - t_1$ (in h^{-1} Myr), respectively, assuming metric parameters $\Omega_m = 0.28, \Omega_r = 1.65 \times 10^{-4}, \Omega_\Lambda = 1 - \Omega_m - \Omega_r$ and the T^3 fundamental axis ($l = 6^\circ, b = +77^\circ$) of length $L = 11.4h^{-1}$ Gpc.

name	l_1	b_1	l_2	b_2	z_1	z_2	Δz	Δt
[SKD2006] 017721	35.597	82.506	174.850	-70.004	5.724	5.281	0.443	75.6
[SKD2006] 036334	36.053	82.455	174.632	-70.020	5.705	5.300	0.405	69.2
[SKD2006] 034503	36.000	82.515	174.771	-69.984	5.698	5.308	0.390	66.6
SDF J132519.4+271829	36.238	82.470	174.368	-69.758	6.000	5.058	0.942	160.2
[SKD2006] 018699	35.605	82.619	175.130	-69.980	5.645	5.356	0.289	49.4
[SKD2006] 020087	35.642	82.613	175.045	-69.917	5.724	5.286	0.438	74.8
[SKD2006] 031858	35.934	82.554	174.870	-69.965	5.692	5.314	0.378	64.5
SDSS J134040.24+281328.1 ^b	41.523	79.054	165.545	-71.950	5.338	5.654	-0.315	-53.9
[SKD2006] 020495	35.635	82.719	175.272	-69.858	5.697	5.314	0.383	65.4
SDF J132426.5+271600	35.900	82.666	174.836	-69.609	6.030	5.039	0.991	168.2
[SKD2006] 023759	35.721	82.737	175.288	-69.846	5.687	5.324	0.363	61.9
[SKD2006] 031765	35.920	82.705	175.167	-69.852	5.691	5.321	0.370	63.1
[SKD2006] 073078	37.030	82.493	174.428	-69.913	5.700	5.314	0.386	65.8
[SKD2006] 027787	35.814	82.765	175.300	-69.801	5.707	5.308	0.399	68.0
[SKD2006] 046904	36.307	82.703	175.075	-69.843	5.665	5.347	0.318	54.2
[SKD2006] 042576	36.182	82.745	175.175	-69.806	5.684	5.331	0.353	60.2
[SKD2006] 039849	36.112	82.767	175.232	-69.788	5.692	5.324	0.368	62.7
[SKD2006] 050215	36.394	82.720	175.070	-69.809	5.682	5.333	0.349	59.4
SDF J132501.3+272628	37.258	82.538	174.767	-70.166	5.337	5.666	-0.329	-56.1
SDF J132442.5+272423	36.992	82.607	174.394	-69.554	6.040	5.038	1.002	169.8
SDF J132345.6+271701	36.019	82.817	175.043	-69.415	6.110	4.986	1.124	190.4
[SKD2006] 061418	36.716	82.675	174.839	-69.763	5.748	5.276	0.472	80.3
[SKD2006] 048328	36.338	82.782	175.196	-69.758	5.693	5.325	0.368	62.6
[SKD2006] 093966	37.603	82.523	174.308	-69.824	5.721	5.302	0.419	71.4
[SKD2006] 070600	36.978	82.784	175.054	-69.738	5.654	5.366	0.288	49.0
[SKD2006] 096007	37.679	82.641	174.544	-69.752	5.696	5.329	0.367	62.5
[SKD2006] 124783	38.436	82.458	173.942	-69.801	5.720	5.308	0.412	70.1
[SKD2006] 095588	37.672	82.650	174.530	-69.710	5.738	5.292	0.446	75.8
[SKD2006] 084305	37.352	82.740	174.832	-69.706	5.695	5.331	0.364	62.0
[SKD2006] 124530	38.442	82.515	174.085	-69.784	5.689	5.337	0.352	59.8
[SKD2006] 084720	37.374	82.768	174.891	-69.695	5.682	5.343	0.339	57.6
[SKD2006] 132343	38.639	82.481	173.954	-69.785	5.697	5.331	0.366	62.3
[SKD2006] 121315	38.376	82.624	174.302	-69.688	5.716	5.317	0.399	67.8
[SKD2006] 113271	38.176	82.675	174.464	-69.673	5.710	5.322	0.388	65.9
[SKD2006] 126848	38.522	82.593	174.197	-69.697	5.718	5.315	0.403	68.4
[SKD2006] 108164	38.033	82.762	174.709	-69.653	5.672	5.358	0.314	53.4
[SKD2006] 152586	39.251	82.713	174.280	-69.578	5.681	5.359	0.322	54.7
[SKD2006] 154296	39.280	82.709	174.235	-69.550	5.715	5.329	0.386	65.5
[SKD2006] 166310	39.595	82.696	174.140	-69.547	5.698	5.346	0.352	59.6
[SKD2006] 158036	39.404	82.755	174.329	-69.540	5.676	5.366	0.310	52.5
[SKD2006] 168127	39.668	82.757	174.268	-69.518	5.674	5.370	0.304	51.4
[SKD2006] 163079	39.556	82.785	174.353	-69.505	5.676	5.368	0.308	52.1
SDSS J133412.56+122020.7 ^b	339.134	72.136	223.205	-77.385	5.134	5.962	-0.828	-139.6
SDSS J140940.72+274507.1 ^c	39.513	72.652	146.699	-75.339	5.359	5.819	-0.460	-76.1

Notes. ^(a) The objects are galaxies except where otherwise indicated. ^(b) QSO. ^(c) Object type uncertain.

2.2.2. Planned and possible observations

First let us consider high-redshift quasars. The VISTA/VIKING 4-m class telescope project should discover quasars at $z \sim 7$ over about 1500 deg² centred on the northern and southern Galactic poles⁴ (Findlay et al. 2011). Although Table 2 here and

the expected completeness levels shown in Fig. 13 of Findlay et al. (2011) indicate that coverage of the desired regions is possible (depending on the value of Ω_m), only about 8 quasars are expected in the whole survey (Sect. 4.1, Findlay et al. 2011), clearly too low to obtain significant evidence either for or against the T^3 candidate.

⁴ The criterion “centred on the northern Galactic cap” presumably means “a large solid angle centred on the northern Galactic pole”.

Polsterer et al. (2012) find 22,992 photometric quasar candidates with $5.5 < z < 6.2$ and an estimated error of $\sigma(\Delta z) =$

0.087, expecting about half the candidates to be true quasars. However, the solid angle from which the quasars are selected is about 2π , giving a candidate surface density of about $1/\text{deg}^2$ and an expected spectroscopic number density of about $0.5/\text{deg}^2$ if a complete spectroscopic followup were to be performed. This is about 100 times higher than for the VISTA/VIKING survey (as presently designed), but still somewhat low. While quasars dominated high-redshift records for the decades when $z > 1$ was considered a high redshift for a spectroscopically confirmed extragalactic object, this seems less likely at $z \sim 6$. For a given apparent magnitude limit, it is clear that LBG and LAE catalogues are present in much high number densities at $z \sim 6$.

Plans for LBG and LAE searches typically focus on the existing “deep fields”, with the aims of achieving wide coverage across the electromagnetic spectrum. Several of these fields and their angular distances θ_i from the closest T^3 axes are given in Table 4, indicating which fields would be the most useful for testing the T^3 candidate via LBG and LAE searches. Comparison with Table 2 indicates that for $5 \lesssim z \lesssim 7$ searches, the Subaru Deep Field and its corresponding northern region is optimal, while for $5.5 \lesssim z \lesssim 8$ searches, the Virgos Very Deep Survey fields 0226–04 and 1400+05 and their northern and southern, respectively, counterparts would be worth observing.

The EUCLID mission⁵ planned for launch in 2019⁶ has a deep survey (Sect. 1.3, Refregier et al. 2010), the EUCLID optical and NIR Deep Imaging Survey, planned over 40 deg^2 . This should obtain “thousands” of likely LBG’s and LAE’s with $z > 6$ based on photometric redshifts (Sect. 14.2, Refregier et al. 2010), i.e., $\gtrsim 50/\text{deg}^2$. If a few objects had quadruple multiplicities that made them very likely topological lensing candidates, then optical/near-infrared spectroscopic followup with an instrument such as X-Shooter (300 nm $\lesssim \lambda \lesssim$ 2400 nm, Vernet et al. 2011) on the Very Large Telescope (VLT) on the southern objects and corresponding spectra of the northern objects with the Keck or Subaru telescopes should obtain enough rest-frame spectral energy distribution information to check whether the would-be topologically lensed pairs of objects resembled each other more than would be expected for arbitrary pairs of objects at similar redshifts. The Multi Unit Spectroscopic Explorer (MUSE)⁷ on the VLT, which should be well-tested by the time that the EUCLID data are available, would be useful for secondary followup to study the spatial environments of the candidate lensed objects, especially when the cosmological time difference between the members of a pair is small compared to a typical galaxy dynamical time scale.

Thus, we should simulate several square degrees of observations with parameters consistent with those estimated for EUCLID. In particular, it would be interesting to see if a statistical signal could be obtained from photometric redshifts alone, prior to spending high amounts of exposure time on highly sought after telescope/instrument combinations.

The Ultra-Deep Survey of the James Webb Space Telescope (JWST) should detect galaxies at $z \gtrsim 6$, but over only about 10 arcmin^2 (Sect. 2, Table II, Gardner et al. 2006). The JWST’s planned Deep Wide Survey should find galaxies over $1 \lesssim z \lesssim 6$ over a larger solid angle, 100 arcmin^2 (Sect. 3.6, Table III, Gardner et al. 2006). For an initial uncertainty of about two degrees in the T^3 axes, these surveys are clearly too narrow.

2.3. Simulations

Simulating searches for type I quadruples requires comparison of observations in a T^3 model to those in an \mathbb{R}^3 model. The existing Subaru Deep Field observations are used to provide an observationally based simulation of both sorts, in which the southern field is generated for the T^3 model by applying the Aurich (2008) T^3 holonomy (Table 1) to the Subaru galaxies, and simulated independently of real observations in the case of the \mathbb{R}^3 model. For a hypothetical observational program aimed at the centres of both the 1–4 axis expected matched discs, fully simulated data are needed in both cases.

The spatial two-point auto-correlation function $\xi(r)$ could, in principle, lead to excess non-topological chance isometries if the tolerances for requiring isometry are not tight enough. For the low number densities of objects expected, the effect is unlikely to be strong. Half of a large number of points are first generated uniformly within a redshift shell defined by the required redshift limits. Each further point is chosen by randomly choosing an existing point, and placing the new point in a 3-Euclidean direction chosen uniformly from 4π ster at a comoving distance chosen with the probability $P(r, dr) \propto 1 + \xi(r)$, where

$$\xi(r) = \begin{cases} \left(\frac{r_0}{r_{\min}}\right)^\gamma, & r \leq r_{\min} \\ \left(\frac{r_0}{r}\right)^\gamma, & r_{\min} \leq r < r_{\max} \\ 0, & r \geq r_{\max}, \end{cases} \quad (2)$$

for a correlation length r_0 and power law index γ , and numerical cutoffs r_{\min} and r_{\max} . Points that do not fall in the redshift shell are ignored, and new points are generated in the same way until the required number fill the shell. Numerical measurement of the resulting simulated distributions shows that in practice, this simulates a stronger correlation than that required. Thus, the chance of non-topological isometries is overestimated, i.e. our results are conservative: real observations are less likely to give a false positive detection. Moreover, in order to err on the side of possibly underestimating the numbers of matching quadruples in the multiply connected case, the correlation function is not used when simulating this case; uniform distributions are drawn from instead. Again, this is conservative: we slightly underestimate the statistical significance of the method (Sect. 2.5).

Peculiar velocities and the uncertainties in redshift estimation need to be simulated (Roukema 1996). Photometric redshift errors are those of most interest here: are they small enough to significantly discriminate between signal and noise? These errors are all simulated radially using a peculiar rapidity ϕ_{pec} selected from a Gaussian distribution of mean zero and standard deviation $\text{atanh}(\sigma(\beta_{\text{pec}}))$ for a single input parameter, the peculiar velocity standard deviation $\sigma(\beta_{\text{pec}})$, and using Eq. (A.4), where $\beta_{\text{pec}} = \tanh \phi_{\text{pec}}$ and $z_{\text{pec}} = [(1 + \beta_{\text{pec}})/(1 - \beta_{\text{pec}})]^{1/2} - 1$. Use of rapidities rather than velocities avoids the unphysical case of $|\beta_{\text{pec}}| \geq 1$ for simulating photometric redshifts with high $\sigma(\beta_{\text{pec}})$.

Before applying the holonomies in a given simulation, random Gaussian errors are added to the T^3 axis parameters given in Table 1. “Observations” of the simulated catalogues are carried out in galactic coordinate limited regions in the expected position(s).

2.4. The successive filter method for type I pairs

Lehoucq et al. (1999) introduced the terminology of type II pairs and type I pairs (or n -tuples), that had been introduced earlier by Lehoucq et al. (1996) and Roukema (1996), respectively. Type I pairs or n -tuples can be thought of as the matching between a

⁵ <http://sci.esa.int/euclid>

⁶ <http://sci.esa.int/science-e/www/object/index.cfm?fobjectid=49385>

⁷ <http://muse.univ-lyon1.fr/>

local region of objects and its distant copy. Since a holonomy for an FLRW multiply connected model is an isometry, the distances among the members within the “original” region should correspond to the distances among the members of the copy of that region. A Type II pair—in a space such as T^3 —corresponds to an object and its copy. In T^3 , this separation is a vector in the covering space \mathbb{R}^3 . Difficulties in finding statistically significant numbers of either type of pair given realistic observational parameters and noise led to a new way of collecting type I pairs (Uzan et al. 1999) and a successive filter method (Marecki et al. 2005). Fujii & Yoshii (2011) presented a variation on the successive filter method, along with an analysis step that is roughly equivalent to collecting together n -tuples of mixed type for all $n \geq 4$ or to the Marecki et al. (2005) bunches of pairs filter (Sect. 3.2.5, Fujii & Yoshii 2011). The latter step, made possible by the successive filters, significantly reduces the combinatorial problem presented in Roukema (1996). A catalogue containing two distant regions, each with N objects, might contain just one pair of matched n -tuples across the two regions, but searching for all $(^N C_n)^2$ combinations of objects with $N = 100$ and $n = 7$ would require 10^{20} comparisons of 7-tuples. Fujii & Yoshii (2011) use toy simulations to show that a very small number of matched n -tuples can be detected by the full method of successive filtering and collecting.

The successive filter method implemented here tests four simulated (and/or real) galaxies at $(x, y, z)(i)$, $(x, y, z)(j)$, $(x, y, z)(k)$, and $(x, y, z)(l)$ via the following filters in the following order, where (i, j, k, l) is an ordered choice of unequal indices in the list of galaxies. A crossed quadruple parameter $\chi(\mathbf{q}) \in \mathbb{Z}_2$ is defined for a given ordered quadruple $\mathbf{q} = (i, j, k, l)$ in order to relate the lifetime and bunches of pairs (BoP) filters (Marecki et al. 2005). This algorithm allows the pair separations d , where $d(.,.)$ is the comoving distance between two arbitrary points in the covering space \mathbb{R}^3 , the (signed) x, y, z component separations of each pair, to be calculated first, and the loop for finding quadruples to be performed over pairs of pairs. Arithmetically, the change from subtraction to addition of pair separations in the BoP filter is equivalent to swapping an $((i, j), (k, l))$ pair of ordered pairs to $((i, k), (j, l))$. The filters are:

(1) type I pair filter:

$$|d(i, j) - d(k, l)| < \epsilon, \quad (3)$$

(2) lifetime filter:

$$\begin{aligned} |t_i - t_k| < \Delta t \text{ and } |t_j - t_l| < \Delta t &\Rightarrow \chi((i, j, k, l)) = 0, \text{ or} \\ |t_i - t_l| < \Delta t \text{ and } |t_j - t_k| < \Delta t &\Rightarrow \chi((i, j, k, l)) = 1, \text{ or} \\ \text{otherwise:} &\text{ filter fails, } \nexists \chi \end{aligned} \quad (4)$$

(3) BoP filter:

$$\begin{aligned} (\chi((i, j, k, l)) = 0 \text{ and } &|[x(i) - x(j)] - [x(k) - x(l)]| < \epsilon_{\text{BoP}} \\ &\text{and } |[y(i) - y(j)] - [y(k) - y(l)]| < \epsilon_{\text{BoP}} \\ &\text{and } |[z(i) - z(j)] - [z(k) - z(l)]| < \epsilon_{\text{BoP}}) \\ \text{or} & \\ (\chi((i, j, k, l)) = 1 \text{ and } &|[x(i) - x(j)] + [x(k) - x(l)]| < \epsilon_{\text{BoP}} \\ &\text{and } |[y(i) - y(j)] + [y(k) - y(l)]| < \epsilon_{\text{BoP}} \\ &\text{and } |[z(i) - z(j)] + [z(k) - z(l)]| < \epsilon_{\text{BoP}}). \end{aligned} \quad (5)$$

Substituting a difference test for the BoP filter above, i.e. $|d(i, j) - d(k, l)| < \epsilon_{\text{BoP}}$ and $|d(i, k) - d(j, l)| < \epsilon_{\text{BoP}}$ for the uncrossed and crossed pairs of pairs, respectively, would allow non-planar quadrilaterals (fold a rectangular sheet of paper along its diagonal to see this), whereas only a parallelogram can represent a T^3 topological quadruple.

A list of quadruples (pairs of pairs, each associated with a crossed quadruple parameter χ) that satisfy all three successive filters is obtained. An arbitrary galaxy i is a member of $s_i \geq 0$ quadruples. The frequency of s in a given simulated set of galaxies is $f(s)$, i.e.

$$f(s) := |\{i : s_i = s\}|. \quad (6)$$

If a topological lensing signal is present, there should be a high number of galaxies which are a member of many quadruples, $f(s)$ should be high for high s . This is a critical step in the successive filter method, introduced in Sect. 3.2.5 of Fujii & Yoshii (2011): for $s \gg 1$, the statistic $f(s)$ should be significantly higher in a catalogue containing topological lensing than in a simply connected catalogue.

2.5. Statistical significance

For an arbitrary realisation, let us define the cumulative number of galaxies that are each members of many quadruples

$$F(s^*) := \sum_{s > s^*} f(s), \quad (7)$$

for some quadruplet membership number $s^* > 0$, which formalises the word “many” in “many quadruples”. Thus, for a fixed value s^* , F is a random variable which we model numerically. To estimate what observational strategy is required to have a low chance of a false negative inference from the data, i.e. to find β , the expected probability of falsely excluding the T^3 hypothesis, suppose that the observational result gives $F = i$ for some non-negative integer i . Then the probability of falsely excluding the Aurich (2008) T^3 hypothesis is the cumulative probability $P(F \leq i | T^3)$, which can be estimated numerically by finding the fraction of T^3 simulations for which $F \leq i$. Since we don’t yet know the results of the observations, we have to weight this (“marginalise it”) over the probability density function of i for the simply connected case.

Thus, the expectation value of the probability of falsely rejecting the hypothesis is

$$p_0 = \sum_{i=0}^{\infty} (p(F = i | \mathbb{R}^3) P(F \leq i | T^3)). \quad (8)$$

Similarly, to estimate what observational strategy is required to have a low chance of a false positive inference from the data, the expected probability of falsely supporting the T^3 hypothesis can

be written

$$\begin{aligned}
& \sum_{i=0}^{\infty} \left(p(F = i|T^3) P(F \geq i|\mathbb{R}^3) \right). \\
&= \sum_{i=0}^{\infty} \left[p(F = i|T^3) \left(\sum_{j=i}^{\infty} p(F = j|\mathbb{R}^3) \right) \right]. \\
&= \sum_{i=0}^{\infty} \sum_{j=i}^{\infty} \left[p(F = i|T^3) \left(p(F = j|\mathbb{R}^3) \right) \right]. \\
&= \sum_{j=0}^{\infty} \sum_{i=0}^j \left[p(F = i|T^3) \left(p(F = j|\mathbb{R}^3) \right) \right]. \\
&= p_0,
\end{aligned} \tag{9}$$

i.e. the two expectation values are equal.

For a given simulation parameter set, a set of simulations is analysed for each $s^* \in \{1, \dots, 10\}$, a range that is found below (Sect. 3) by inspection of $N(s)$ versus s histograms for typical realisations. The minimum

$$p_1 := \min_{s^*} p_0 \tag{10}$$

determines the s^* value for the optimal statistical test for the simulation parameter set, and the expectation value of the probability of falsely excluding the T^3 hypothesis or of falsely detecting evidence in favour of it.

3. Results

3.1. Existing observations

Table 5 lists observed objects and the implied positions where topologically lensed images should be observed if the T^3 hypothesis is correct, with zero uncertainty in the T^3 axis parameters given in Table 1). Figure 3 shows the application of the successive filters method under the assumption that a survey of one square degree in the redshift range $5 < z < 6.2$ is 100% complete in comparison to the surveys that found the high galactic latitude sample. The southern survey field is centred on the expected median celestial position of the implied objects (the fourth and fifth columns of Table 5). The topological signal is clearly very strong in Fig. 3, both for low $\Delta t = 0.01 h^{-1}$ Gyr (top), in which case it is unlikely that stellar evolution would cause the earlier image of a galaxy to dim too much to be seen, and for high $\Delta t = 1 h^{-1}$ Gyr, in which case dimming could weaken the test. The northern part of each catalogue analysed consists of the 44 known objects, there are 41 topologically implied objects within the southern field, and the simulated southern subset consists of 24 and 30 objects for $\Delta t = 0.01 h^{-1}$ Gyr and $1 h^{-1}$ Gyr, respectively.

The uncertainty in the T^3 coordinates and fundamental length also need to be taken into account. An error of 2° in the vector (in the flat comoving covering space) from the observer to an object at a matched disc centre implies an error of about twice the size in the observing angle of the implied image, because the diameter of the shell containing objects at the distance of the matched disc centres is twice the radius of the shell. Thus, as Fig. 4 shows, a typical realisation of a 1 deg^2 southern survey is very unlikely to detect any topological quadruples (satisfying the filter criteria). The total disappearance of the topological signal in this figure ($s = 0$ for all objects, since there are no topological images lying within the southern field at all), making the $N(s)$ distribution even weaker than that of the simply connected

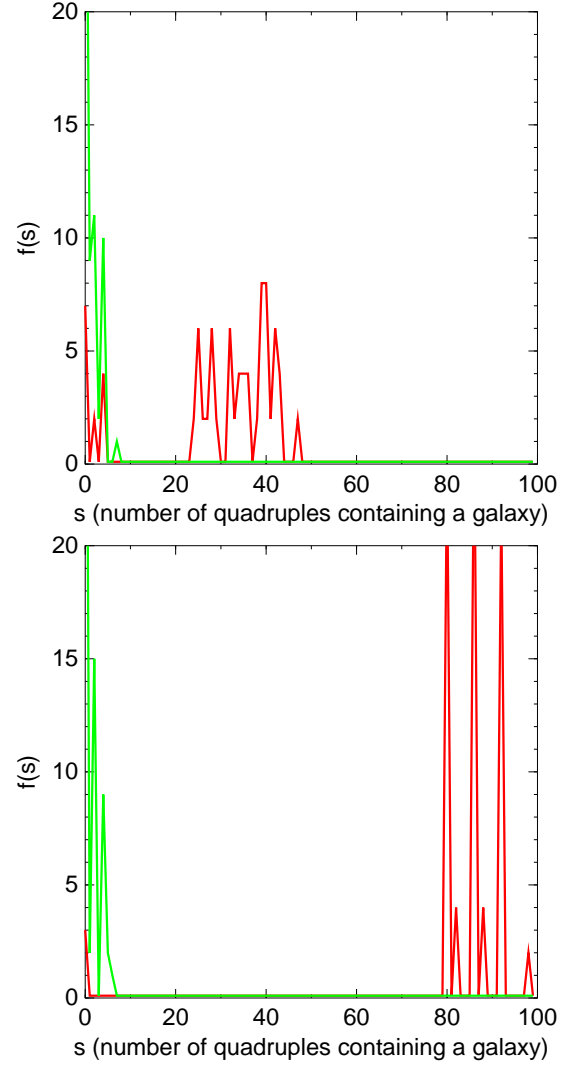


Fig. 3. Quadruple frequencies $N(s)$ obtained by the successive filter method (Sect. 2.4) applied to sets of objects in the multiply connected (dark curve, red online) and simply connected (pale curve, green online) cases, using the known, northern galactic objects in the SDF (second, third and sixth columns of Table 5). The southern object set is calculated using the Aurich (2008) T^3 model in the multiply connected case, and simulated with an input auto-correlation function $r_0 = 10.0 h^{-1}$ Mpc, $\gamma = 1.8$, $r_{\min} = 1.0 h^{-1}$ Mpc, $r_{\max} = 100.0 h^{-1}$ Mpc in the simply connected case. The southern field is “observed” over 1 deg^2 at the expected position in both cases. *Top:* Successive filter parameters (Sect. 2.4) are $\epsilon = 1.0 h^{-1}$ Mpc, $\Delta t = 0.01 h^{-1}$ Gyr, $\epsilon_{\text{BOP}} = 1.0 h^{-1}$ Mpc. *Bottom:* Same, except that $\Delta t = 1 h^{-1}$ Gyr.

data set, is an artefact of the method. We did not add any “background” simulated data around the northern galactic, observed SDF field, so the implied southern objects constitute a “survey” that contains less objects (zero) than the simulated southern survey (16 objects in Fig. 4). Thus, let us consider fully simulated surveys.

3.2. Planned or possible observations

Given the uncertainties in the T^3 solution discussed in Sect. 2.1 and listed in Table 1, let us consider a pair of northern and southern surveys centred on the matched disc centres for the same T^3 axis, each of 64 deg^2 . As explained above, for a given known object, a two degree T^3 axis uncertainty yields an approximately

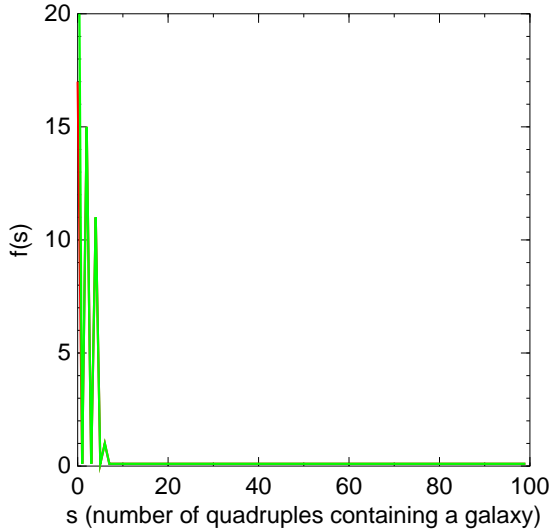


Fig. 4. Quadruple frequencies $N(s)$, as for Fig. 3, but a realisation of Gaussian uncertainties in the T^3 parameters is applied, destroying the topological signal, since none of the implied topological images fall in the southern field in this realisation.

four degree uncertainty for an observer placed halfway between the opposing images and searching for a topological image at the expected position. However, since we simulate both fields, other pairs of objects in the matched discs can be found, so 2° should approximately correspond to a 68% chance (for one angle offset from a Gaussian distribution of width 2°) of finding matching pairs. Thus, 64 deg^2 should approximately correspond to a 2σ (where σ is one standard deviation) chance of finding topological pairs.

The uncertainty in L^{T^3} gives a 1σ uncertainty of about $150 h^{-1} \text{ Mpc}$, i.e. a 2σ uncertainty of $300 h^{-1} \text{ Mpc}$. For a survey going from the matched disc centre to $\beta \approx 4^\circ$ away, Table 2 (for $\Omega_m = 0.28$) gives a typical redshift of $z \approx 5.38$, i.e. $5.706 h^{-1} \text{ Gpc}$ in radial comoving distance from the observer. Inverting this, $5706 \pm 300 h^{-1} \text{ Mpc}$ gives $4.60 \lesssim z \lesssim 6.33$. We extend this a little to be conservative, and increase the filter criterion ϵ to $2 h^{-1} \text{ Mpc}$. A typical realisation is shown in the top panel of Fig. 5. Clearly, a pair of surveys that are wide enough on the sky and in redshift coverage, finding 300 objects above an idealised, z -independent completeness limit, has a good chance of strongly rejecting or supporting the T^3 hypothesis.

Could photometric redshift estimates be sufficient? The lower panel of Fig. 5 shows the quadruple signal for a realisation with Gaussian peculiar velocity uncertainties simulated with $\sigma(\beta_{\text{pec}}) = 0.005$, i.e. a redshift uncertainty of $\sigma(\Delta z) \approx 0.03$. The signal is clearly much weaker, but (in this realisation) is still distinguishable from the $N(s)$ curve of the simply connected simulation.

Figure 6 presents confidence levels, i.e. p_1 , as defined in Eq. (10) in Sect. 2.5, from ensembles of realisations. Unsurprisingly, low $\sigma(\Delta z_{\text{phot}})$ and high N_{gal} generally give the statistically most significant results. The dependence on these two parameters is not fully monotonic. This is understandable because for a fixed $\sigma(\Delta z_{\text{phot}})$, higher N_{gal} not only increases the numbers of topological quadruples, it also increases the number density, so that the numbers of non-topological quadruples also increase, yielding some complexity in the dependence. There is some statistical noise in the contours. The total computing time for Fig. 6 on a single, recent 4-core processor would be from a few weeks to a few months (Appendix B). The actual calculations were per-

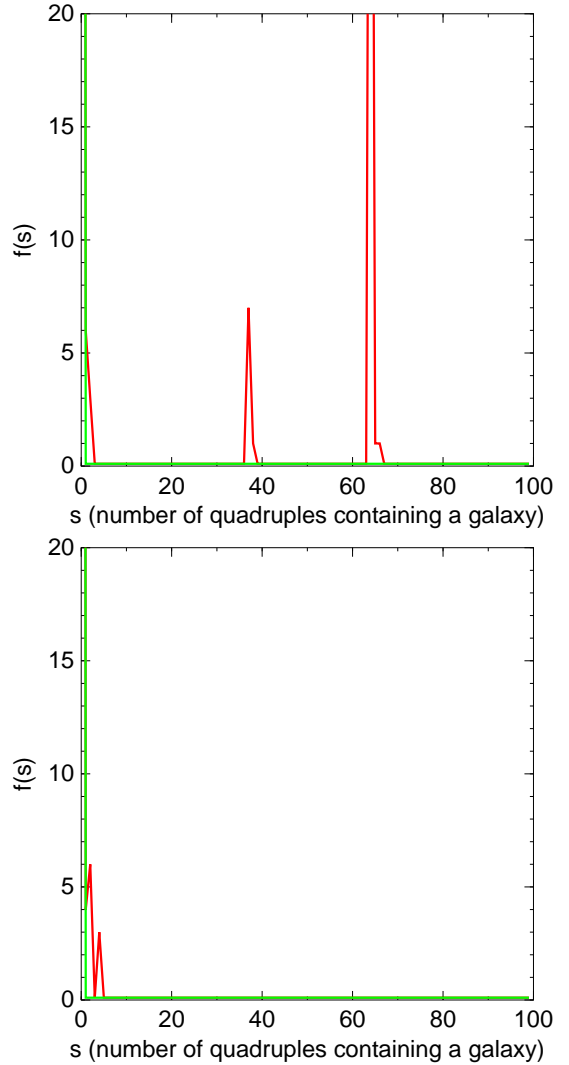


Fig. 5. As for Fig. 3, for fully simulated, multiply connected (dark, red online) and simply connected (pale, green online) catalogues, over northern and southern fields each of $\approx 64 \text{ deg}^2$ centred at antipodal matched disc centres, with $4.3 < z < 6.6$, and successive filter parameters $\epsilon = 2.0 h^{-1} \text{ Mpc}$, $\Delta t = 1.0 h^{-1} \text{ Gyr}$, $\epsilon_{\text{BoP}} = 1 h^{-1} \text{ Mpc}$, and (in the simply connected case) an input auto-correlation function $r_0 = 10.0 h^{-1} \text{ Mpc}$, $\gamma = 1.8$, $r_{\text{min}} = 1.0 h^{-1} \text{ Mpc}$, $r_{\text{max}} = 100.0 h^{-1} \text{ Mpc}$ [Eq. (2)]. A total of 300 simulated objects (north plus south) are present in each catalogue. *Top*: Spectroscopic redshifts. *Bottom*: Photometric redshifts with $\sigma(\beta_{\text{pec}}) = 0.005$, i.e. $\sigma(\Delta z) \approx 0.03$.

formed using parallel computing resources on several different machines.

Figure 6 also shows that a typical photometric redshift error of $\sigma(\Delta z_{\text{phot}}) \lesssim 0.01$ would enable rejection at $p_1 \lesssim 0.05$ (i.e. a 2σ rejection according to intuition for a Gaussian distribution), provided that $N_{\text{gal}} \gtrsim 500$ in northern and southern surveys each over $\omega \approx 100 \text{ deg}^2$. This is only a moderate confidence level for rejecting the hypothesis, but since p_1 also represents the expectation value of falsely accepting the hypothesis, it would be sufficient to provide a strong motivation for studying candidate topologically lensed galaxies further. A plot roughly similar to the lower panel of Fig. 5 would be obtained, enabling the particular galaxies most likely to be topologically lensed to be identified. The particular realisation in the lower panel of Fig. 5 shows about 10 galaxies that are each members of $s > 1$ quadruples.

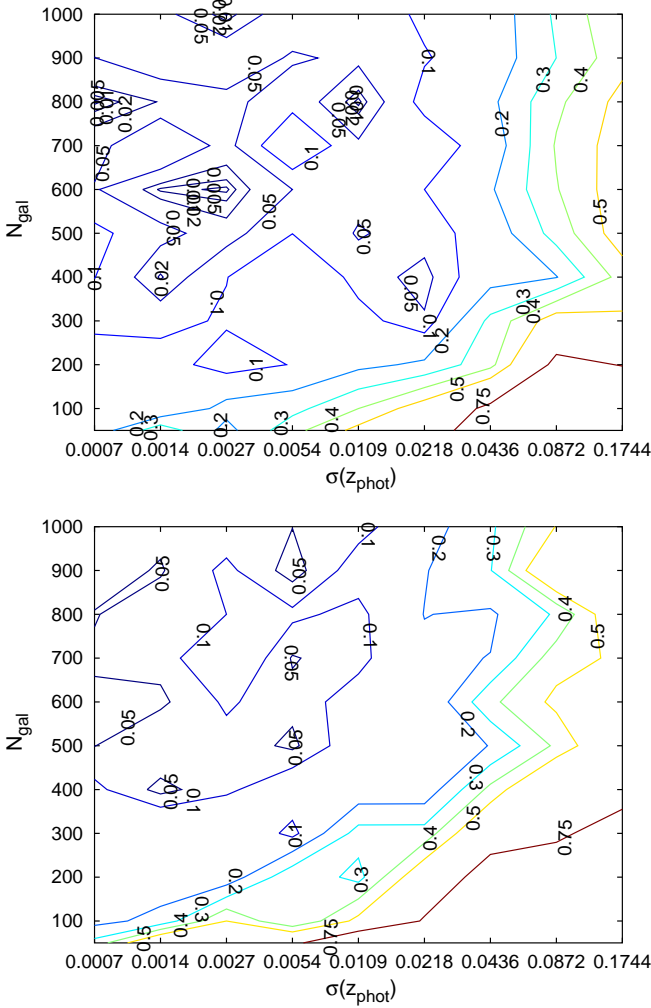


Fig. 6. Expectation values p_1 of falsely rejecting (or falsely accepting) the T^3 hypothesis for optimal choices of s^* [Eq. (10)], as a function of photometric redshift $\sigma(z_{\text{phot}})$ [estimated as $(1 + (z_1 + z_2)/2)\sigma(\beta_{\text{pec}})$, using $\sigma(\beta_{\text{pec}}) \ll 1$ and Eq. (A.4), where $z_1 < z < z_2$ is the redshift range], and the number of galaxies N_{gal} per combined (north plus south) catalogue. The lowest probabilities p_1 (highest significance) results are for low $\sigma(z_{\text{phot}})$ and high N_{gal} , at top-left in each of the panels. *Top:* $4.3 < z < 6.6$, solid angle per survey direction (south or north) $\omega \approx 100 \text{ deg}^2$, $\Delta t = 1 h^{-1} \text{ Gyr}$. The other parameters are identical to those for Fig. 5. *Bottom:* Same, except that $\Delta t = 0.1 h^{-1} \text{ Gyr}$.

This is a small enough number for spectroscopic followup to be relatively easy to obtain.

Comparison of the top and bottom panels in Fig. 6 illustrates the potential role of evolutionary effects. The lower panel limits type II pairs to those with $\Delta t = 0.1 h^{-1} \text{ Gyr}$ instead of $\Delta t = 1 h^{-1} \text{ Gyr}$ (upper panel). To attain moderate confidence, i.e. $p_1 \lesssim 0.05$, photometric redshift errors would need to be tightened to about $\sigma(\Delta z_{\text{phot}}) \lesssim 0.005$, for slightly higher numbers of galaxies. For initial starburst durations not much shorter than a typical galaxy dynamical time of $\sim 1 h^{-1} \text{ Gyr}$, $\Delta t = 0.1 h^{-1} \text{ Gyr}$ should give a high probability that a galaxy is included in a survey at both its topological images.

Figure 7 shows that increasing the survey area and redshift depth still further, to $\omega \approx 196 \text{ deg}^2$ and $4 < z < 7$, would allow statistically similar results for weaker accuracy of the photometric redshifts and lower numbers of galaxies. An accuracy of $\sigma(z_{\text{phot}}) \lesssim 0.02$ or $\sigma(z_{\text{phot}}) \lesssim 0.01$, for $\Delta t = 1 h^{-1} \text{ Gyr}$ (upper

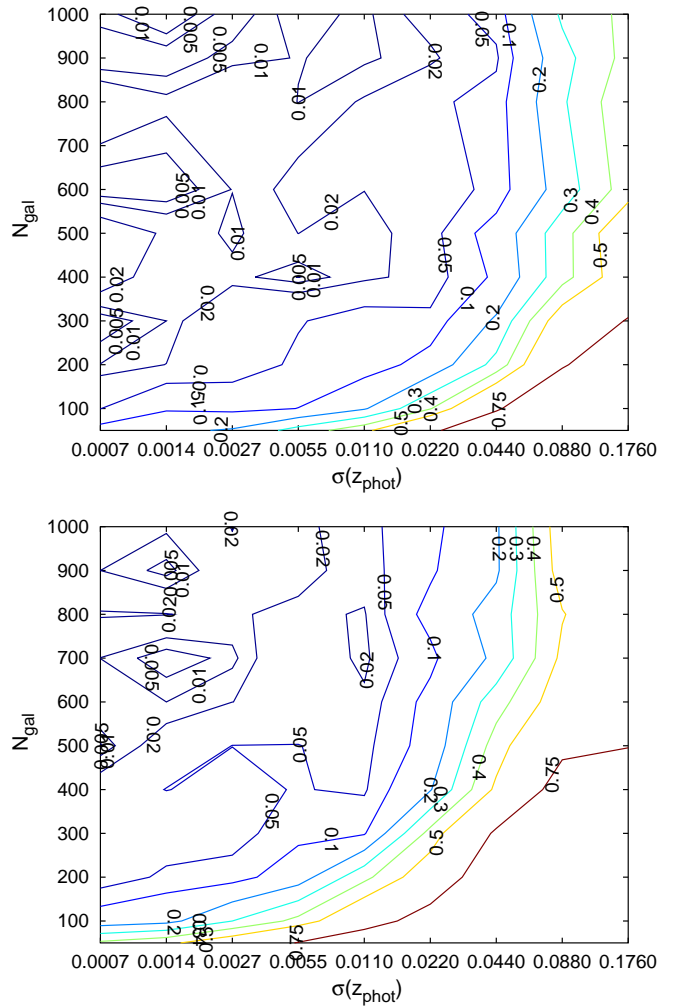


Fig. 7. Expectation values p_1 of falsely rejecting (or falsely accepting) the T^3 hypothesis, as for Fig. 6, but for a thicker, wider survey, over $4 < z < 7$ and $\omega \approx 196 \text{ deg}^2$. *Top:* $\Delta t = 1 h^{-1} \text{ Gyr}$, *Bottom:* $\Delta t = 0.1 h^{-1} \text{ Gyr}$.

panel) or $\Delta t = 0.1 h^{-1} \text{ Gyr}$ (lower panel), respectively, would give $p_1 \lesssim 0.05$.

Figure 7 also shows that for a sufficiently high number of galaxies, $N_{\text{gal}} \gtrsim 900$, a photometric redshift accuracy of $\sigma(\Delta z_{\text{phot}}) \lesssim 0.01$ would be sufficient for $p_1 \lesssim 0.01$, i.e. an expectation value of false rejection of about 1%. Most of the present interest in photometric redshift techniques is at lower redshifts, but high statistical accuracy in $z \sim 6$ photometric redshifts would clearly be useful for deep redshift topological lensing.

4. Conclusion

Over the next few decades, wide-angle surveys in the $z \sim 6$ redshift range will inevitably be performed. The results above indicate that with appropriate targetting and choices of observational parameter limits, the speed with which the T^3 candidate for the topology of the Universe can be rejected or detected can be optimised. For more specific observational strategies for particular telescope/instrument combinations, more detailed analyses could potentially be carried out by using detailed galaxy formation models, such as the hybrid N -body/semi-analytic simulations (Roukema et al. 1993, 1997, 2001) that have been extensively developed to simulate detailed galaxy properties as a

function of space and time (e.g., Hatton et al. 2003, and references thereof), including a specific focus on LAEs (e.g., Garel et al. 2012). More sophisticated combinations of existing observations, including the VVDS 1400+05 field within 16° of the same southern axis and the VVDS 0226–04 field within 20° of the corresponding northern axis (Table 4) along with simulated future observations, should also potentially yield several alternative strategies for topological lensing detection or rejection.

The total number of L_* galaxies at $4 \leq z \leq 7$, where L_* is the characteristic luminosity of a Schechter function (Schechter 1976), is estimated to be $\phi_* \sim 3 \times 10^{-3} h^3 \text{ Mpc}^{-3}$ (e.g. Table 5, Bouwens et al. 2011). This gives about 3–8 million L_* galaxies for the pairs of 100 deg^2 and 196 deg^2 fields simulated above, over $4.3 < z < 6.6$ and $4 < z < 7$, respectively. For the minimum $N_{\text{gal}} \gtrsim 500$ or $N_{\text{gal}} \gtrsim 400$ needed for achieving 5% expected confidence levels in the two field sizes, respectively (Sect. 3.2), surveys complete to $L \gtrsim 8.8L_*$ or $L \gtrsim 9.9L_*$, respectively, would find the required numbers of galaxies. Because the computing time for the above calculations scales roughly as N_{gal}^4 for sufficiently high N_{gal} (since the heaviest computation is checking the list of possible quadruples; see Appendix B), simulations for surveys complete to $L \gtrsim L_*$, i.e. for $N_{\text{gal}} \gtrsim 10^6$, are clearly not practical without further filters added early in the successive filter algorithm.

Nevertheless, the most difficult aspect of predicting constraints on the model is the difference between *precise* cosmology and *accurate* cosmology. The dark energy parameter Ω_Λ is suspected to be an artefact of using the FLRW metric (a homogeneous solution of the Einstein equation) rather than the physical average metric of the actually inhomogeneous Universe (e.g. Buchert & Carfora 2003; Buchert 2008; C  lerier et al. 2010; Wiegand & Buchert 2010). A significant confirmation of the T^3 hypothesis would provide a constraint on the inhomogeneous approach to cosmology, but this is unlikely to occur using an FLRW interpretation of the observational data if the time dependence of the FLRW metric parameters is too far from relativistically consistent formulae in the relevant redshift range (Larena et al. 2009). Some of the familiar FLRW relations may be algebraically valid in fully relativistic models, with an effective rather than a local physical interpretation (Buchert & R  s  nen 2012), so detection of topological lensing might still be possible under the assumption of an FLRW metric.

Acknowledgements. Thank you to Roland Bacon for contributing several key ideas to this project. Some of this work was carried out within the framework of the European Associated Laboratory “Astrophysics Poland-France”. BFR thanks the Centre de Recherche Astrophysique de Lyon for a warm welcome and scientifically productive hospitality. A part of this project has made use of Program Oblicze n Wielkich Wyzwa n nauki i techniki (POWIEW) computational resources (grant 87) at the Pozna n Supercomputing and Networking Center (PCSS). A part of this work was conducted within the “Lyon Institute of Origins” under grant ANR-10-LABX-66. Use was made of the Centre de Donn  es astronomiques de Strasbourg (<http://cdsads.u-strasbg.fr>), the GNU PLOTUTILS graphics package, and the GNU OCTAVE command-line, high-level numerical computation software (<http://www.gnu.org/software/octave>).

References

Aslanyan, G., & Manohar, A. V. 2012, *J. Cosmology Astropart. Phys.*, 6, 3, [arXiv:1104.0015]
 Aurich, R. 2008, *ClassQuantGra*, 25, 225017, [arXiv:0803.2130]
 Aurich, R., Janzer, H. S., Lustig, S., & Steiner, F. 2008, *Classical and Quantum Gravity*, 25, 125006, [arXiv:0708.1420]
 Aurich, R., Lustig, S., & Steiner, F. 2005a, *ClassQuantGra*, 22, 3443, [arXiv:astro-ph/0504656]
 Aurich, R., Lustig, S., & Steiner, F. 2005b, *ClassQuantGra*, 22, 2061, [arXiv:astro-ph/0412569]

Aurich, R., Lustig, S., & Steiner, F. 2010, *ClassQuantGra*, 27, 095009, [arXiv:0903.3133]
 Aurich, R., Lustig, S., Steiner, F., & Then, H. 2004, *Classical and Quantum Gravity*, 21, 4901, [arXiv:astro-ph/0403597]
 Aurich, R., Lustig, S., Steiner, F., & Then, H. 2007, *ClassQuantGra*, 24, 1879, [arXiv:astro-ph/0612308]
 Bennett, C. L., Halpern, M., Hinshaw, G., et al. 2003, *ApJS*, 148, 1, [arXiv:astro-ph/0302207]
 Bielewicz, P., & Banday, A. J. 2011, *MNRAS*, 412, 2104, [arXiv:1012.3549]
 Block, D. L. 2011, *ArXiv e-prints*, [arXiv:1106.3928]
 Bouwens, R. J., Illingworth, G. D., Oesch, P. A., et al. 2011, *ApJ*, 737, 90, [arXiv:1006.4360]
 Buchert, T. 2008, *General Relativity and Gravitation*, 40, 467, [arXiv:0707.2153]
 Buchert, T., & Carfora, M. 2003, *PRL*, 90, 031101, [arXiv:gr-qc/0210045]
 Buchert, T., & R  s  nen, S. 2012, *Annual Review of Nuclear and Particle Science*, 62, 57, [arXiv:1112.5335]
 Caillerie, S., Lach  ze-Rey, M., Luminet, J.-P., et al. 2007, *A&A*, 476, 691, [arXiv:0705.0217v2]
 C  lerier, M., Bolejko, K., & Krasinski, A. 2010, *A&A*, 518, A21, [arXiv:0906.0905]
 Copi, C. J., Huterer, D., Schwarz, D. J., & Starkman, G. D. 2007, *Phys. Rev. D*, 75, 023507, [arXiv:astro-ph/0605135]
 Copi, C. J., Huterer, D., Schwarz, D. J., & Starkman, G. D. 2009, *MNRAS*, 399, 295, [arXiv:0808.3767]
 Copi, C. J., Huterer, D., Schwarz, D. J., & Starkman, G. D. 2010, *Advances in Astronomy*, 2010, 847541, [arXiv:1004.5602]
 Cornish, N. J., Spergel, D. N., & Starkman, G. D. 1996, *ArXiv Gen.Rel. & Quant.Cosm. e-prints*, [arXiv:gr-qc/9602039]
 Cornish, N. J., Spergel, D. N., & Starkman, G. D. 1998, *ClassQuantGra*, 15, 2657
 Davis, M., Guhathakurta, P., Konidaris, N. P., et al. 2007, *ApJ*, 660, L1, [arXiv:astro-ph/0607355]
 de Sitter, W. 1917, *MNRAS*, 78, 3
 Ducout, A., Bouchet, F. R., Colombi, S., Pogosyan, D., & Prunet, S. 2012, *MNRAS*, 423, [arXiv:1209.1223]
 Findlay, J. R., Sutherland, W. J., Venemans, B. P., et al. 2011, *ArXiv e-prints*, [arXiv:1111.3314]
 Friedmann, A. 1923, *Mir kak prostranstvo i vremya* (The Universe as Space and Time) (Petrograd: Academia)
 Friedmann, A. 1924, *Zeitschr. f  r Phys.*, 21, 326
 Fujii, H., & Yoshii, Y. 2011, *A&A*, 529, A121, [arXiv:1103.1466]
 Gardner, J. P., Mather, J. C., Clampin, M., et al. 2006, *Space Sci. Rev.*, 123, 485, [arXiv:astro-ph/0606175]
 Garel, T., Blaizot, J., Guiderdoni, B., et al. 2012, *MNRAS*, 422, 310, [arXiv:1202.0610]
 Gundermann, J. 2005, *ArXiv e-prints*, [arXiv:astro-ph/0503014]
 Hatton, S., Devriendt, J. E. G., Ninin, S., et al. 2003, *MNRAS*, 343, 75, [arXiv:astro-ph/0309186]
 Iovino, A., McCracken, H. J., Garilli, B., et al. 2005, *A&A*, 442, 423, [arXiv:astro-ph/0507668]
 Key, J. S., Cornish, N. J., Spergel, D. N., & Starkman, G. D. 2007, *Phys. Rev. D*, 75, 084034, [arXiv:astro-ph/0604616]
 Lach  ze-Rey, M., & Luminet, J. 1995, *Phys. Rep.*, 254, 135, [arXiv:gr-qc/9605010]
 Larena, J., Alimi, J.-M., Buchert, T., Kunz, M., & Corasaniti, P.-S. 2009, *Phys. Rev. D*, 79, 083011, [arXiv:0808.1161]
 Le F  vre, O., Vettolani, G., Maccagni, D., et al. 2003, *The Messenger*, 111, 18
 Lehnert, M. D., Nesvadba, N. P. H., Cuby, J.-G., et al. 2010, *Nature*, 467, 940, [arXiv:1010.4312]
 Lehoucq, R., Lach  ze-Rey, M., & Luminet, J.-P. 1996, *A&A*, 313, 339, [arXiv:gr-qc/9604050]
 Lehoucq, R., Luminet, J.-P., & Uzan, J.-P. 1999, *A&A*, 344, 735, [arXiv:astro-ph/9811107]
 Lema  tre, G. 1927, *Annales de la Soci  t   Scientifique de Bruxelles*, 47, 49
 Lema  tre, G. 1931, *MNRAS*, 91, 483
 Luminet, J., & Roukema, B. F. 1999, in *NATO ASIC Proc. 541: Theoretical and Observational Cosmology*. Publisher: Dordrecht: Kluwer., ed. M. Lach  ze-Rey, 117, [arXiv:astro-ph/9901364]
 Luminet, J., Weeks, J. R., Riazuelo, A., Lehoucq, R., & Uzan, J. 2003, *Nature*, 425, 593, [arXiv:astro-ph/0310253]
 Luminet, J.-P. 1998, *Acta Cosmologica*, XXIV-1, 105, [arXiv:gr-qc/9804006]
 Luminet, J.-P. 2006, *Brazilian Journal of Physics*, 36, 107, [arXiv:astro-ph/0501189]
 Maihara, T., Iwamuro, F., Tanabe, H., et al. 2001, *PASJ*, 53, 25, [arXiv:astro-ph/0009409]
 Marecki, A., Roukema, B. F., & Bajtlik, S. 2005, *A&A*, 435, 427, [arXiv:astro-ph/0412181]

Narlikar, J. V. 1994, *American Journal of Physics*, 62, 903

Niarchou, A., & Jaffe, A. 2007, *PRL*, 99, 081302, [arXiv:astro-ph/0702436]

Picard, E. 1884, *Bull. Soc. Math. France*, 12, 43, http://www.numdam.org/item?id=BSMF_1884__12__43_0

Polsterer, K. L., Zinn, P.-C., & Gieseke, F. 2012, *MNRAS*, 10, [arXiv:1210.7071]

Rebouças, M. J., & Gomero, G. I. 2004, *Braz. J. Phys.*, 34, 1358, [arXiv:astro-ph/0402324]

Refregier, A., Amara, A., Kitching, T. D., et al. 2010, *ArXiv e-prints*, [arXiv:1001.0061]

Robertson, H. P. 1935, *ApJ*, 82, 284

Roukema, B. F. 1996, *MNRAS*, 283, 1147, [arXiv:astro-ph/9603052]

Roukema, B. F. 2000, *Bull. Astr. Soc. India*, 28, 483, [arXiv:astro-ph/0010185]

Roukema, B. F. 2010, *MNRAS*, 404, 318, [arXiv:0911.1205]

Roukema, B. F., Buliński, Z., & Gaudin, N. E. 2008a, *A&A*, 492, 657, [arXiv:0807.4260]

Roukema, B. F., Buliński, Z., Szaniewska, A., & Gaudin, N. E. 2008b, *A&A*, 486, 55, [arXiv:0801.0006]

Roukema, B. F., & Kazimierczak, T. A. 2011, *A&A*, 533, A11, [arXiv:1106.0727]

Roukema, B. F., Ninin, S., Devriendt, J., et al. 2001, *A&A*, 373, 494, [arXiv:astro-ph/0105152]

Roukema, B. F., Peterson, B. A., Quinn, P. J., & Rocca-Volmerange, B. 1997, *MNRAS*, 292, 835, [arXiv:astro-ph/9707294]

Roukema, B. F., Quinn, P. J., & Peterson, B. A. 1993, in *Astronomical Society of the Pacific Conference Series*, Vol. 51, *Observational Cosmology: an International Symposium*, Milano, Italy, 21–25 September 1992, ed. G. L. Chin-carini, A. Iovino, T. Maccacaro, & D. Maccagni, 298

Sarkar, D., Huterer, D., Copi, C. J., Starkman, G. D., & Schwarz, D. J. 2011, *Astroparticle Physics*, 34, 591, [arXiv:1004.3784]

Schechter, P. 1976, *ApJ*, 203, 297

Schmalzing, J., & Buchert, T. 1997, *ApJ*, 482, L1, [arXiv:astro-ph/9702130]

Schmalzing, J., & Gorski, K. M. 1998, *MNRAS*, 297, 355, [arXiv:astro-ph/9710185]

Shimasaku, K., Kashikawa, N., Doi, M., et al. 2006, *PASJ*, 58, 313, [arXiv:astro-ph/0602614]

Spergel, D. N., Verde, L., Peiris, H. V., et al. 2003, *ApJS*, 148, 175, [arXiv:astro-ph/0302209]

Starkman, G. D. 1998, *ClassQuantGra*, 15, 2529

Starobinsky, A. A. 1993, *JETPLett*, 57, 622

Stevens, D., Scott, D., & Silk, J. 1993, *PRL*, 71, 20

Synge, J. 1960, *Relativity: The General Theory* (Amsterdam: North-Holland)

Uzan, J.-P., Lehoucq, R., & Luminet, J.-P. 1999, *A&A*, 351, 766, [arXiv:astro-ph/9903155]

van den Bergh, S. 2011, *JRASC*, in press, [arXiv:1106.1195]

Vernet, J., Dekker, H., D’Odorico, S., et al. 2011, *A&A*, 536, A105, [arXiv:1110.1944]

Wiegand, A., & Buchert, T. 2010, *Phys. Rev. D*, 82, 023523, [arXiv:1002.3912]

Williams, R. E., Blacker, B., Dickinson, M., et al. 1996, *AJ*, 112, 1335, [arXiv:astro-ph/9607174]

Appendix A: Combination of cosmological and peculiar velocities in the FLRW model

As derived in Synge (1960) and presented in Narlikar (1994) (see also Roukema 2010, and refs therein), the expansion redshift can be derived by parallel-transporting the four-velocity of the world line of a distant galaxy along a null geodesic (path of a photon) joining it to the observer. A fundamental observer (at rest with respect to the comoving spatial coordinate system) has zero peculiar velocity and a redshift of z_{cosm} . The latter can be interpreted as a special-relativistic radial speed β_{cosm} in natural units, where

$$\begin{aligned}
 1 + z_{\text{cosm}} &= \sqrt{\frac{1 + \beta_{\text{cosm}}}{1 - \beta_{\text{cosm}}}} \\
 &= \frac{1}{\gamma_{\text{cosm}}(1 - \beta_{\text{cosm}})} \\
 &= \gamma_{\text{cosm}}(1 + \beta_{\text{cosm}}) \\
 &= \cosh \phi_{\text{cosm}} + \sinh \phi_{\text{cosm}} \\
 &= e^{\phi_{\text{cosm}}},
 \end{aligned} \tag{A.1}$$

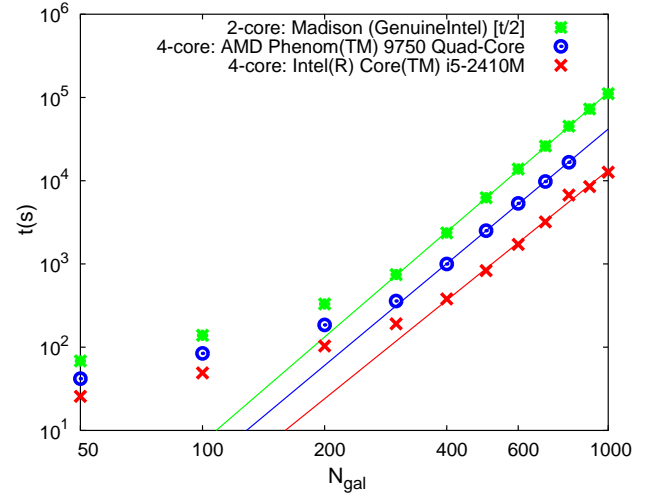


Fig. A.1. Confidence level calculation time in seconds for quadruple searches of (the equivalent of) 30 realisations for a single parameter set, as a function of the total number of galaxies N_{gal} , for the simulations shown in Figs 6 and 7, for three different processor sets, as labelled. The times for the first processor set are halved to give the equivalent of four cores. Power-law fits to $N_{\text{gal}} \geq 400$ are shown.

where ϕ_{cosm} is the rapidity defined by $\beta_{\text{cosm}} = \tanh \phi_{\text{cosm}}$, $\gamma_{\text{cosm}} := (1 - \beta_{\text{cosm}}^2)^{-1/2}$, and $\gamma_{\text{pec}} := (1 - \beta_{\text{pec}}^2)^{-1/2}$. For a radial peculiar velocity of β_{pec} in natural units, the overall redshift z can be calculated using Minkowski spacetime addition of the rapidities ϕ_{cosm} and ϕ_{pec} , where $\beta_{\text{pec}} = \tanh \phi_{\text{pec}}$, i.e. the overall rapidity is

$$\phi = \phi_{\text{cosm}} + \phi_{\text{pec}}, \tag{A.2}$$

since addition of four-velocity vectors at the same spacetime location is meaningful. Thus, similarly to Eq. (A.1), the overall redshift is given by

$$\begin{aligned}
 1 + z &= e^{\phi} \\
 &= e^{\phi_{\text{cosm}} + \phi_{\text{pec}}} \\
 &= (1 + z_{\text{cosm}})(1 + z_{\text{pec}}),
 \end{aligned} \tag{A.3}$$

i.e.

$$z = z_{\text{cosm}} + z_{\text{pec}} + z_{\text{cosm}}z_{\text{pec}}. \tag{A.4}$$

When $\max(z_{\text{cosm}}, |z_{\text{pec}}|) \ll 1$, this reduces to $z = z_{\text{cosm}} + z_{\text{pec}}$ to first order in both redshifts.

For high-redshift astronomy, i.e. $z_{\text{cosm}} > 1$, the third term in the right-hand side of Eq. (A.4) is more significant than the second, contrary to popular belief that sets the third term to zero. Nevertheless, for $|z_{\text{pec}}| \ll 1$, which is realistic even for low-redshift astronomy, Eq. (A.4) can be approximated to first order in β_{pec} ,

$$z \approx z_{\text{cosm}} + \beta_{\text{pec}} + z_{\text{cosm}}\beta_{\text{pec}}. \tag{A.5}$$

We ignore gravitational redshift here, since observations close to the Schwarzschild radius are unlikely in the case of interest. Parallel transport of the four-velocity (see Narlikar 1994) implies analogous relations to those above.

Appendix B: Simulation benchmarking

Figure A.1 shows that for sufficiently high N_{gal} , the successive filter quadruple searches scale roughly as the fourth power of the

number of simulated galaxies. From top to bottom as labelled, the power law best fits are proportional to $N_{\text{gal}}^{4.2}$, $N_{\text{gal}}^{4.1}$, and $N_{\text{gal}}^{3.9}$, respectively. Parallelisation is via OPENMP.